Energy Storage Materials xxx (xxxx) xxx–xxx

Contents lists available at ScienceDirect

Energy Storage Materials

journal homepage: www.elsevier.com/locate/ensm

Porous insulating matrix for lithium metal anode with long cycling stability and high power

Bingqing Xu[a,b], Haowei Zhai[a], Xiangbiao Liao[c], Boyu Qie[a], Jyotirmoy Mandal[a], Tianyao Gong[a], Laiyuan Tan[a], Xiujia Yang[a], Kerui Sun[a], Qian Cheng[a], Meijie Chen[a], Yupeng Miao[d], Mian Wei[d], Bin Zhu[a], Yanke Fu[a], Aijun Li[a], Xi Chen[c], Wei Min[d], Ce-Wen Nan[b,*], Yuan-Hua Lin[b,*], Yuan Yang[a,*]

[a] *Program of Materials Science and Engineering, Department of Applied Physics and Applied Mathematics, Columbia University, New York, 10027, United States*
[b] *State Key Laboratory of New Ceramics and Fine Processing, School of Materials Science and Engineering, Tsinghua University, Beijing, 100084, PR China*
[c] *Yonghong Zhang Family Center for Advanced Materials for Energy and Environment, Department of Earth and Environmental Engineering, Columbia University, New York, 10027, United States*
[d] *Department of chemistry, Columbia University, New York, 10027, United States*

ARTICLE INFO

Keywords:
Lithium metal anode
Porous polymer matrix
Phase-field simulations

ABSTRACT

Lithium metal anode has great potential for high-energy-density lithium batteries due to its high theoretical capacity, but its practical applications are limited by the uncontrollable growth of lithium dendrites. In this work, we fabricate a facile 3D porous polymer structure with one-step phase inversion method and verify the structure by Stimulated Raman Scattering Microscopy. Such 3D porous structure leads to uniform lithium plating and striping, improving the electrochemical performance remarkably. In Li/Cu cell tests, the porous structure modified Cu delivers high Coulombic Efficiency (CE) of 96% after 240 cycles at 1 mA/cm^2, while bare Cu drops to less than 20% after 42 cycles. As for Li/Li cell tests, it delivers stable cycling over 1275 cycles with only 200 mV over potential at 3 mA/cm^2 and 1 mAh/cm^2 in Li/Li cells. At as high as 4 mA/cm^2, it delivers more than 200 cycles with less than 200 mV. With PVdF-HFP interfacial layer, it could hold up to 4 mAh/cm^2, it delivers more than 110 hours at 4 mA/cm^2 and 4 mAh/cm^2. The as-assembled $LiFePO_4$/porous polymer/lithium full cell shows stable capacity around 153 mAh/g and no obvious voltage polarization over 350 cycles at 0.5 C. The stable cycling performance can be attributed to the lower current density from the large specific surface area of as-deposited lithium in porous polymer matrix and confined dendrite growth path in 3D porous structure.

1. Introduction

Rechargeable lithium metal batteries (LMBs) with high energy density have been considered as promising electrochemical storage systems, since the lithium metal anode has high specific capacity and very negative electrode potential [1–7]. However, the uncontrollable growth of lithium dendrites during cycling results in significant obstacles to the applications of LMBs, because such undesired lithium dendrites directly lead to the breakdown of solid electrolyte interphase (SEI), fast electrolyte consumption, short-circuit and even thermal runaway [8–12].

Various methods have been reported to suppress the growth of lithium dendrites recently, such as surface capping layer [13,14], 3D conductive skeleton [15], 3D framework design [16–18], current collector architecture [19–21], artificial solid electrolyte interphase [22,23], interlayer design [24], separator modification [25], advanced electrolytes and additives [26–29], and solid ceramic and polymer electrolytes [30–34]. To suppress dendrite growth for practical applications, an easy, scalable and effective approach to realize stable lithium deposition is still highly desired [35].

Inspired by the porous sponge structure, we attempt to develop 3D porous structure to guide lithium stripping and plating. The high tortuosity in porous structures increase pathway for lithium to grow, and reduce the chance to form long dendrite to penetrate battery separators. Moreover, the higher surface area of lithium in 3D porous structure is also expected to extend the cycling life by decreasing the effective current density on lithium surface (Fig. 1**a**). In addition, unlike conductive matrix, the insulating nature of polymer limits the deposition

* Corresponding authors.
E-mail addresses: cwnan@mail.tsinghua.edu.cn (C.-W. Nan), linyh@tsinghua.edu.cn (Y.-H. Lin), yy2664@columbia.edu (Y. Yang).

https://doi.org/10.1016/j.ensm.2018.11.035
Received 24 October 2018; Received in revised form 30 November 2018; Accepted 30 November 2018

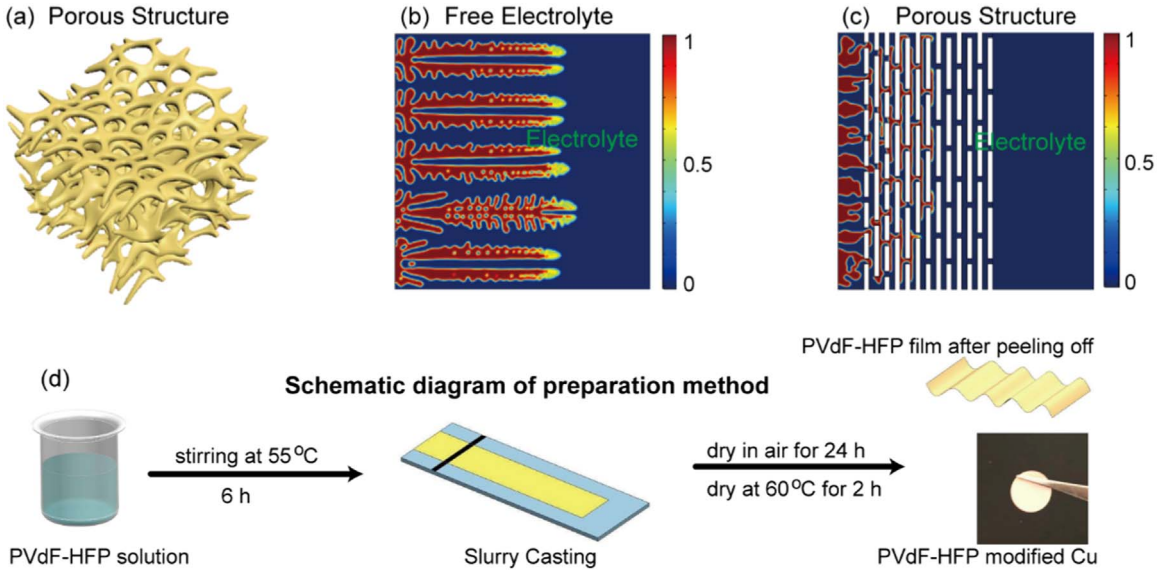

Fig. 1. The design of porous PVdF-HFP matrix, phase field simulation, and sample preparation. a) A schematic diagram of the 3D porous structure design. b, c) COMSOL simulations of the lithium dendrite growth process in b) free electrolyte and c) porous structure modified lithium foil. 0 and 1 mean electrolyte and lithium metal, respectively. d) The preparation process of PVdF-HFP film by the phase inversion method.

of lithium directly on the top surface of such porous skeleton. In this report, we find that such 3D porous structure is effective in suppressing dendrite growth. The lithium anode modified by such porous structure delivers as long as 1200 cycles even at 3 mA/cm^2 and 1 mAh/cm^2. Moreover, the full cell assembled with $LiFePO_4$ cathode is cycled over 350 cycles steadily at 0.5 C with a high capacity of 153 mAh/g.

2. Material and methods

2.1. Materials

$LiFePO_4$ powders and EC/DEC electrolyte (1 M $LiPF_6$ in ethylene carbonate (EC) /diethyl carbonate (DEC) (1:1 v/v)) were purchased from Gotion and used as received. Super C65 carbon black was from Timcal. Kynar 761 PVDF and PVdF-HFP were received from Arkema. Lithium bis(trifluoromethanesulfonyl)imide (LiTFSI) was received from Solvay. 1,3-dioxolane (DOL) and 1,2- dimethoxyethane (DME) were purchased from Sigma Aldrich.

2.2. PVdF-HFP film preparation

Firstly, PVdF-HFP, acetone and water were mixed in a weight ratio of 1:8:1, and stirred for 6 hours at 55 °C. Then the solution was casted onto an acid-cleaned copper foil (15 min in 5 wt% H_2SO_4). Then it was dried in the fume hoods for 12 hours at room temperature and then transferred in the oven at 60 °C for 2 hours. The film is cut into discs.

Battery fabrication: Li/Cu cells were assembled in EC/DEC (1 M $LiPF_6$ in EC/DEC (1:1 v/v)) and DOL/DME electrolyte (1 M LiTFSI in DOL/DME (1:1 v/v), 1 wt% $LiNO_3$). The electrolyte volume was fixed at 40 µl. Li/Li cells were fabricated both in carbonate and DOL/DME electrolyte, and the electrolyte volume is also fixed at 40 µl. The full cell test was carried out with the $LiFePO_4$ cathode at a capacity of 1.4 mAh/cm^2 in the DOL/DME electrolyte and the electrolyte volume is fixed at 60 µl. The $LiFePO_4$ electrode was prepared by casting a slurry with $LiFePO_4$, Super C65 and PVDF in a weight ratio of 8:1:1 in 1-Methyl-2-pyrrolidone (NMP) and dried at 110 °C in vacuum. All the cells were assembled in a glovebox with O_2 and H_2O less than 0.5 ppm.

2.3. Electrochemical measurements

The galvanostatic cycling was performed with Land Battery testers. The Li/Cu cells were tested in EC/DEC and DOL/DME electrolyte at a capacity of 1 mAh/cm^2 and at current density of 0.25, 0.5, 1, 2.5 mA/cm^2. Li/Li cells were tested both in carbonate and DOL/DME electrolyte. Li/Li cells were tested at different current densities and capacities. Electrochemical Impedance Spectroscopy (EIS) was tested by a Bio-Logic SAS VMP3 tester from 1 MHz to 0.1 Hz.

2.4. SEM, spontaneous Raman, stimulated Raman Scattering Microscopy (SRS) characterizations

The microstructure images were collected from a Zeiss Sigma VP scanning electron microscope. Spontaneous Raman spectra were acquired in the range of 2800–3200 cm^{-1} using an upright confocal Raman spectrometer (Xplora; HORIBA Jobin Yvon), with a 532 nm laser. The setup of SRS microscopy characterization was done with 8 MHz modulated Stokes beam at 1064 nm, and Pump beam at 805.2 nm, whose energy difference corresponds to 3020 cm^{-1}. The SRS set up details are as described previously [7]. The film is soaked in isopropanol (IPA) to render it transparent. Peak at 3020 cm^{-1} was chosen to detect the C-H distribution of PVdF-HFP. The 3D structure is reconstructed using surfaces rendering in the Imaris software [36].

2.5. Non-linear phase field simulation methods

1) A simple electrodeposition is considered, Li^+A^- cations in a dilute electrolyte solution reacting with electrons at the electrode surface. The Gibbs free energy of the system can be expressed by

$$G = \int^V [f_h(\tilde{C}) + f_{grad}(\nabla\tilde{C}) + f_{elec}(\tilde{C},\phi)]dV$$

in which $\tilde{C} = \{\tilde{c} = \frac{c}{c_s}, \tilde{c}_+ = \frac{c_+}{c_0}, \tilde{c}_- = \frac{c_-}{c_0}\}$ is the set of dimensionless concentration for Li-atom, Li^+ cation and A^- anion respectively. c_s is the site density of Li-metal and c_0 represents the bulk concentration of dilute electrolyte. $f_h(\tilde{C}) = g(C) + f_{grad} = \nabla\tilde{C} \bullet (k(\theta)\nabla\tilde{C})/2$ is the gradient energy density to characterize the surface energy. Due to the anisotropy of Li-metal, the orientation-dependent gradient coefficient is introduced here. $f_{elec} = \rho_e\phi$ is the electrostatic potential in which ρ_e is the charge density and ϕ is the electrostatic potential. A phase-field variable, $\xi = \tilde{c}$ corresponding to the dimensionless concentration of Li-atom, is introduced and its value changes from 1 to 0 in the interface.

The phase field is considered to evolve by the electrochemical reaction:

$$\frac{\partial \xi}{\partial t} = R_e = -\kappa_0 \tilde{c}_+^{1-\alpha} a_M \left\{ \exp\left[\frac{(1-\alpha)F\eta}{RT}\right] - \exp\left[\frac{-\alpha F\eta}{RT}\right] \right\}$$

where κ_0 is the reaction rate constant; $0 < \alpha < 1$ is the asymmetry factor; η is the overpotential; a_M is the activity for Li-atom. And the temporal evolution of phase field variable is

$$\frac{\partial \xi}{\partial t} = -L_\sigma(g'(\xi) - k(\theta)\nabla^2\xi) - L_h h'(\xi)\left\{ \exp\left[\frac{(1-\alpha)F\eta_a}{RT}\right] - \exp\left[\frac{-\alpha F\eta_a}{RT}\right] \right\}$$

where $h(\xi) = \xi^3(6\xi^2 - 15\xi + 10)$ is used for interpolating; $\eta_a = \Delta\phi - E^\Theta$ is the activation overpotential; L_σ and L_h are the interfacial mobility and the reaction-related constant.

2) For Li cation diffusing in the electrolyte with electrochemical reaction at the interface, we can describe the diffusion by

$$\frac{\partial \tilde{c}_+}{\partial t} = \nabla \cdot \left[D^{eff} \nabla \tilde{c}_+ + \frac{D^{eff} \tilde{c}_+}{RT} F \nabla \phi \right] - c_s/c_0 \frac{\partial \xi}{\partial t}$$

where the effective diffusion coefficient $D^{eff} = D^e h(\xi) + D^s(1 - h(\xi))$; D^e and D^s are the Li cation diffusion coefficient in the electrode and electrolyte respectively.

3) For electrostatic potential, it should obey Poisson equation

$$\nabla \cdot [\sigma^{eff} \nabla \phi] = F c_s / c_0 \frac{\partial \xi}{\partial t}$$

where the source term relates to the reaction rate at interface.

The phase-field evolution is simulated through COMSOL 5.2. All the parameters refer the previous study. The system 400 × 400μm with minimum size of 0.5 μm and adaptive timestep is modeled. Initial Li metal protuberants with small size are introduced to initialize dendrite growth [37].

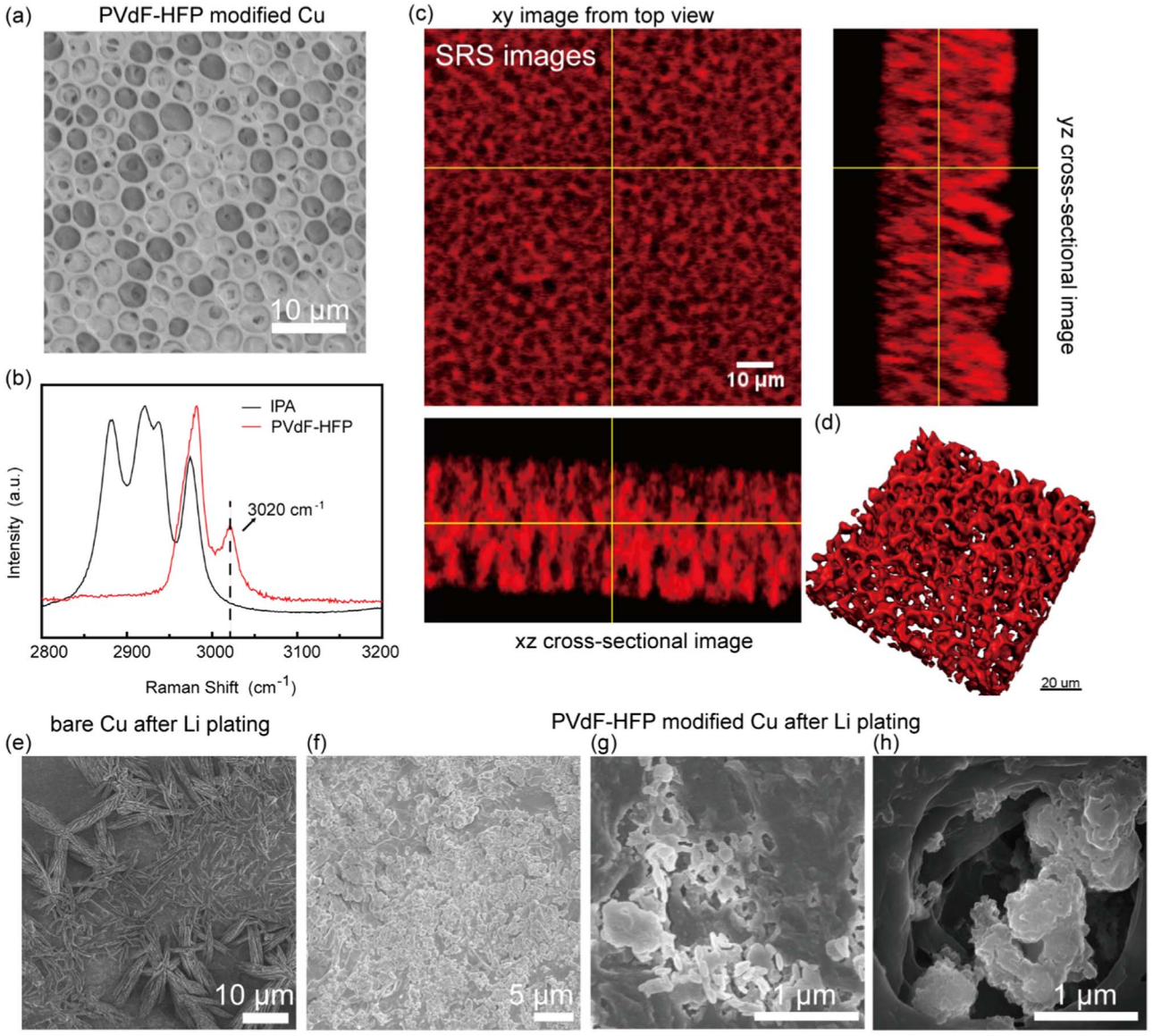

Fig. 2. a) An SEM image of porous PVdF-HFP structure coated Cu substrate. It shows pores with diameter of 2–3 μm. b) Spontaneous Raman spectrums of isopropanol (IPA) and PVdF-HFP in the range of 2800–3200 cm^{-1}. The peak 3020 cm^{-1} is characteristic of PVdF-HFP. c) An SRS image at the depth of 20 μm from top view xy image, and cross-sectional views, yz and xz cross-sectional images, it shows the film is porous from top and cross-sectional view. d) Surface-rendered 3D SRS image of PVdF-HFP film. e) An SEM image of lithium metal deposited on bare Cu after the first deposition. f-h) SEM images of PVdF-HFP modified Cu after 1st lithium deposition at different magnifications. It shows that the holes are uniformly filled with lithium. It could be seen easily that lithium prefers to be deposited in the holes. More SEM images can be found in Figure S3.

3. Results and discussion

The effectiveness of porous insulating structure is first investigated by simulation. The lithium deposition process in free electrolyte and porous structure is simulated in 2D by the phase field method (Fig. 1**b/c**). When a current of 1 mA/cm^2 is applied, obvious growth of lithium dendrite is observed at a speed of 10.5 μm/min in the free electrolyte (Fig. 1**b**). In contrast, when a porous structure with impermeable wall is added in, the growth rate is reduced to 4.5 μm/min (Fig. 1**c**). Such large contrast proves the effectiveness of porous insulating matrix (e.g. polymer) to suppress dendrite growth.

To experimentally verify such hypothesis, the proposed 3D porous structure is first prepared by the phase-inversion method, which is a scalable room-temperature solution process (Fig. 1**d**). Specifically, PVdF-HFP and water are dissolved in acetone with a weight ratio of 1:1:8, and then drop cast onto a copper foil. During acetone evaporation, PVdF-HFP precipitates out and wraps around water microdroplets. The water microdroplets finally evaporate and leave voids to render PVdF-HFP porous. From the SEM image, we can clearly see porous structure with size of 2–5 μm. Energy Dispersive X-ray Spectroscopy (EDS) also shows uniform distribution of F and C in the porous structure (Figure S2). To further characterize the 3D structure of the porous PVdF-HFP film, confocal Stimulated Raman Scattering Microscopy (SRS) was used to map the distribution of Raman scattering intensity at 3020 cm^{-1}, which is a representative fingerprint of PVdF-HFP (Fig. 2**b**). As shown in the Fig. 2**d**, the 3D image corresponds to the distribution of PVdF-HFP, which shows clear interconnected porous structure (Fig. 2**d, Movie 1**). A single image at the depth of 20 μm captured is shown as Fig. 2**c**, which shows uniform pores distribution as in SEM results (Fig. 2**c**).

Supplementary material related to this article can be found online at doi:10.1016/j.ensm.2018.11.035.

To verify that lithium can be readily deposited inside the porous structure instead of forming a film under the porous membrane, the porous PVdF-HFP membrane after 1 mAh/cm^2 lithium deposition is further examined by SEM. Firstly, dendrites are clearly formed on the bare copper substrate (Fig. 2**e**). On the other side, the lithium deposition tends to be particle-like lithium clusters instead of needle-like dendrites in porous PVdF-HFP (Fig. 2**f and g**). Lithium can be clearly seen inside holes with size of hundreds of nanometers (Fig. 2**h**). But with increased amount of deposited lithium, the lithium would ultimately fill holes and start to deposit on top of the PVdF-HFP film (Figure S7). Therefore, the PVdF-HFP thickness should be optimized for given capacity of lithium, so that lithium will not penetrate the entire PVdF-HFP film to avoid shorting. In addition to SEM images, the porous PVdF-HFP film also leads to longer deposition time before cell shorting. For example, a bare Cu/separator/Li cell is shorted after 52 hours at 1 mA/cm^2, while porous PVdF-HFP modified Cu/separator/Li cell is shorted after 98 hours at the same current density (Fig. 3**a**). These observations confirm that such porous structure stabilizes the lithium deposition without forming dendrites, which is consistent with the simulation results (Fig. 1**c**).

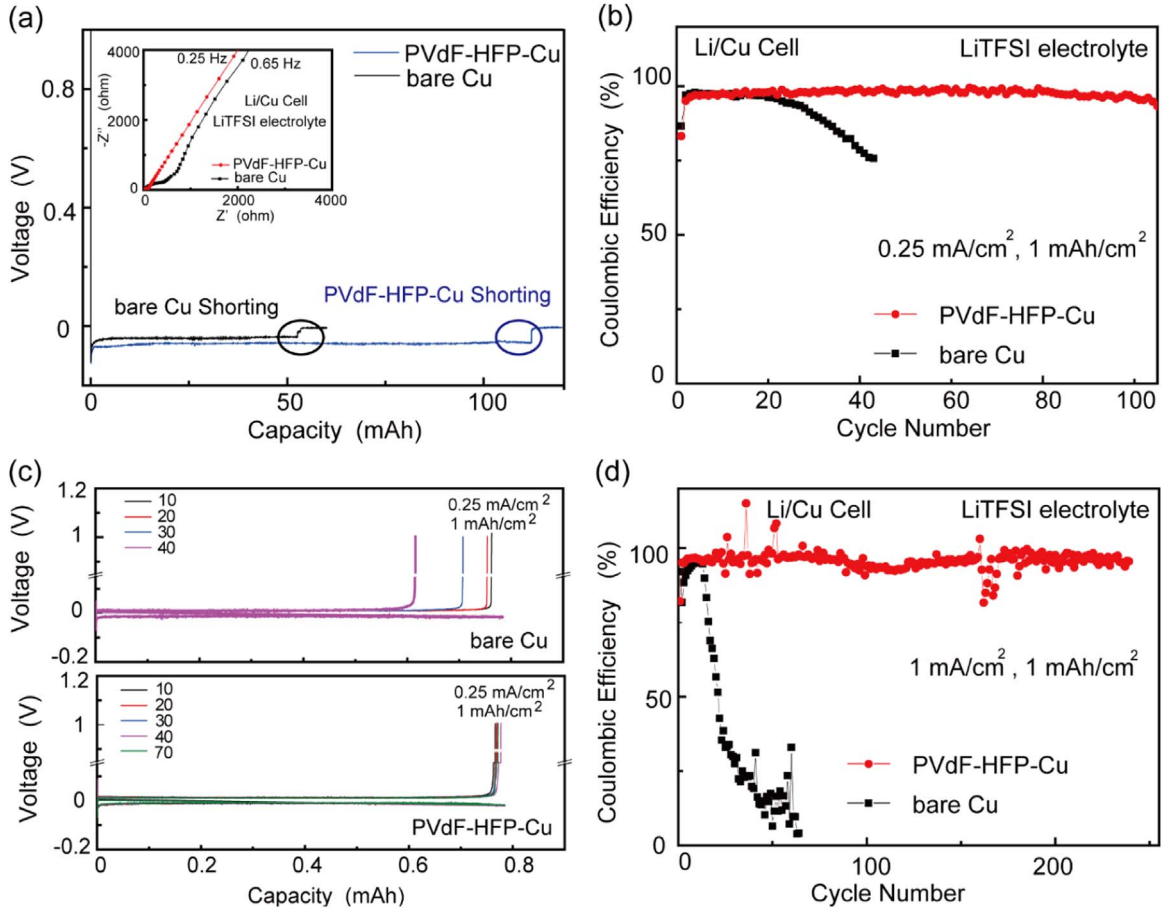

Fig. 3. a) Long-term lithium deposition onto bare Cu and PVdF-HFP modified Cu at 1 mA/cm^2 with continuous discharging. Bare Cu/lithium cell is shorted after 52 hours, while PVdF-HFP-Cu/lithium cell is shorted after 98 hours. Inset: Comparison of impedances of fresh Li/Cu cells assembled with bare Cu and PVdF-HFP-Cu in DOL/DME electrolyte. b) Comparison of the Coulombic efficiency of bare Cu and PVdF-HFP-Cu in DOL/DME electrolyte at different current densities: at 0.25 mA/cm^2, 1 mAh/cm^2. The red curve is PVdF-HFP-Cu and the black curve is bare Cu. c) The voltage-capacity curves of lithium/bare Cu cells after 10, 20, 30 and 40 cycles (top) and the lithium/PVdF-HFP-Cu cells after 10, 20, 30, 40 and 70 cycles at 0.25 mA/cm^2, 1 mAh/cm^2 (bottom). d) Coulombic efficiency comparison of bare Cu and PVdF-HFP modified Cu at 1 mA/cm^2 with a total capacity of 1 mAh/cm^2. (For interpretation of the references to color in this figure legend, the reader is referred to the web version of this article).

To characterize the utilization efficiency of lithium during stripping and plating processes, the Coulombic efficiencies (CE) of bare Cu and PVdF-HFP modified Cu (PVdF-HFP-Cu) are measured in a Li/Cu cell and compared (Fig. 3**b**). 40 µl DOL/DME electrolyte (1 M lithium bis(trifluoromethanesulfonyl)imide (LiTFSI) in 1:1 v/v 1,3-dioxolane (DOL)/1,2-dimethoxyethane (DME) with 1 wt% $LiNO_3$) is used in this test. Mechanical tests show that after soaking with organic electrolytes, the Young's modulus and tensile strength of the porous PVdF-HFP film are reduced from 159 MPa and 6.0 MPa to 11.1 MPa and 3.1 MPa in carbonate electrolyte (1 M $LiPF_6$ in EC/DEC) or 10.3 MPa and 3.1 MPa in ether electrolyte (1 M LiTFSI in DOL/DME), respectively. Meanwhile, the fracturing strain increases from ~120% to beyond ~250%, as shown in Figure S9**.** After soaking in either carbonate or ether electrolyte, the pores still remain, as shown in Figure S10. At a current density of 0.25 mA/cm^2 and lithium deposition of 1 mAh/cm^2, the CE of bare Cu drops abruptly after 20 cycles and remains less than 75% after 40 cycles, indicating low reversible lithium utilization, which may be attributed to dendrite growth from non-uniform contact between copper, electrolyte and separator. Comparatively, the PVdF-HFP-Cu remains a CE of more than 98% for over 80 cycles and keeps stable after 100 cycles. So it is clear that the porous PVdF-HFP coating could stabilize the lithium deposition without evident lithium dendrite. The cycling performance at a current density of 0.5 mA/cm^2 is also tested with 1 mAh/cm^2 deposited (Figure S4). The PVdF-HFP-Cu shows much better cycling performance than bare Cu, with a high average CE of 96% even over 80 cycles. In contrast, the CE for bare Cu drops to less than 50% after 60 cycles. In the voltage-capacity profile (Fig. 3**c** and S5), we can see that in bare Cu, as the cycles increasing, less and less lithium could be stripped from the copper, indicating a lower CE. On the other side, the voltage-capacity profiles almost overlap with each other in PVdF-HFP-Cu, corresponding to enhanced CE. More tests at higher currents of 1 and 2.5 mA/cm^2 show the same trend (Fig. 3**d** and S4). For example, at 1 mA/cm^2, the PVdF-HFP-Cu shows a high CE around 96% even after 240 cycles, but bare Cu drops to less than 20% after 42 cycles. At 2.5 mA/cm^2, the PVdF-HFP-Cu shows a high CE of around 91% for 50 cycles. In contrast, the CE of bare Cu drops quickly to less than 75% in 40 cycles. Such improved performance in PVdF-HFP-Cu compared to bare Cu further supports that the porous PVdF-HFP structure leads to more uniform deposition, so that there is less side reactions between lithium metal and the electrolyte. Besides DOL/DME electrolyte, Li/Cu cells with EC/DEC electrolyte are also tested both at 0.5 and 1 mA/cm^2 with a capacity density of 1 mAh/cm^2 (Figure S6). At 1 mA/cm^2, 1 mAh/cm^2, the CE of bare Cu drops quickly under 40% only after 53 cycles, but the CE of PVdF-HFP-Cu remains over than 80% even after 143 cycles. It confirms that the porous PVdF-HFP film improves cell performance in both ether and EC/DEC electrolyte.

The effectiveness of this porous structure is further investigated in lithium/lithium symmetric cells. PVdF-HFP modified lithium (PVdF-HFP-Li) cells display much more stable cycling performance than bare lithium cells at all current densities and deposited capacity (Fig. 4). For example, at 3 mA/cm^2 and 1 mAh/cm^2, the PVdF-HFP-Li shows steady cycling up to 900 hours, or 1350 cycles, while the voltage of bare lithium cell starts to fluctuate after only 30 h. At 2 mA/cm^2 and

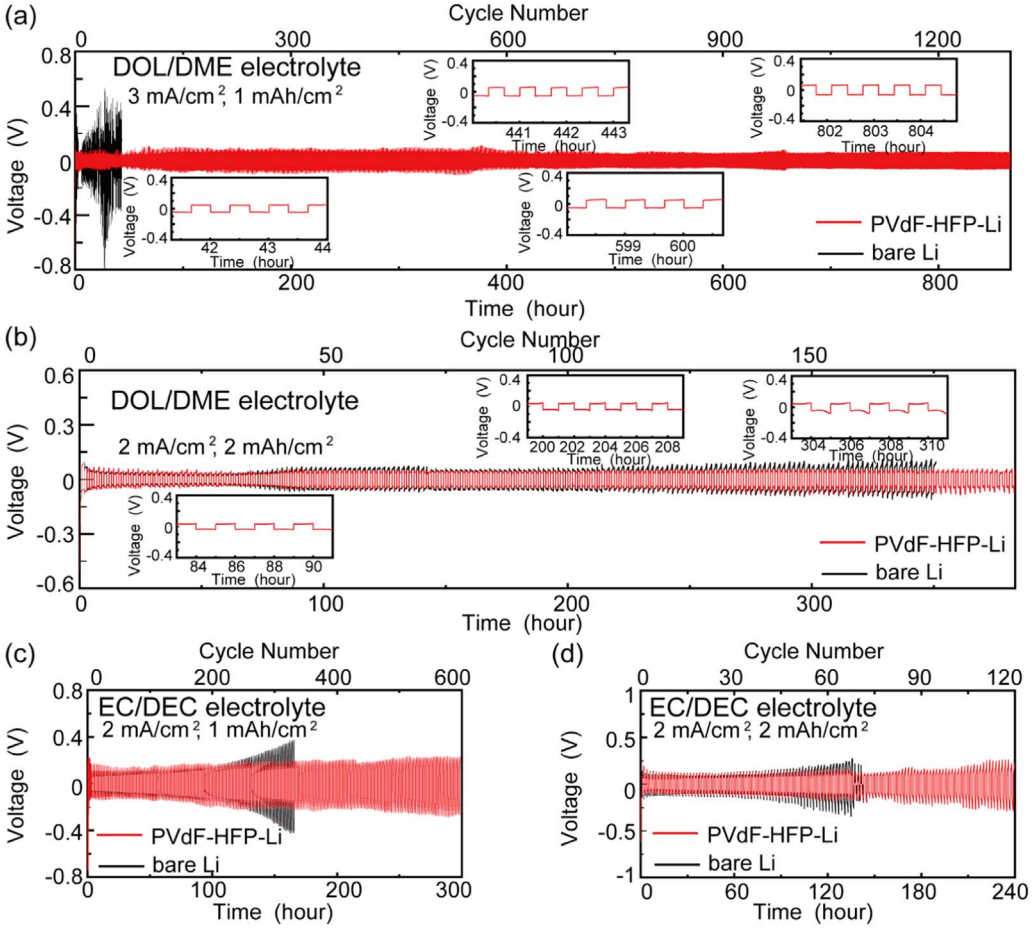

Fig. 4. a-b) Long term Li/Li cycling in DOL/DME electrolyte (1 M LiTFSI in DOL/DME). **a)** Long-term cycling performance of Li/Li cells at 3 mA/cm^2, 1 mAh/cm^2. The red curve is PVdF-HFP-Li and the black curve is bare Li. The inset images correspond to Voltage-Time curves at different times. **b)** Cycling performance of Li/Li cells at 2 mA/cm^2, 2 mAh/cm^2. **c-d)** Li/Li cycling performance comparison of PVdF-HFP-Li and bare Li in EC/DEC electrolyte (1 M $LiPF_6$ in ethylene carbonate (EC) /diethyl carbonate (DEC) (1:1 v/v)) at different conditions: c) 2 mA/cm^2, 1 mAh/cm^2. d) 2 mA/cm^2, 2 mAh/cm^2.

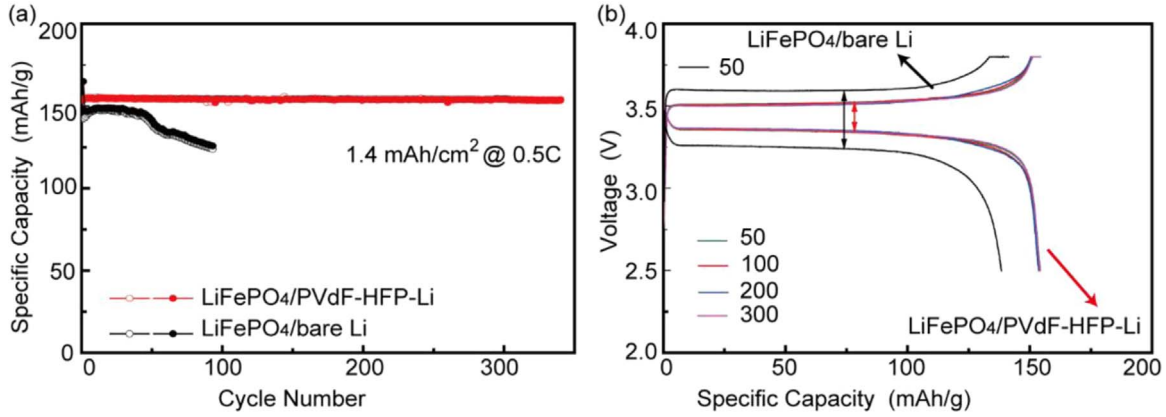

Fig. 5. a) Cycling performance and b) voltage profile of a $LiFePO_4$/Li cell with 1.4 mAh/cm^2 $LiFePO_4$ electrode. The red curve is a $LiFePO_4$/PVdF-HFP-Li cell and the black curve is a $LiFePO_4$/bare Li cell.

1 mAh/cm^2, the PVdF-HFP-Li is stable for over 1000 h, or 1000 cycles, while the voltage of bare lithium cell becomes fluctuating after less than 150 h. Moreover, at 2 m A/cm^2, 2 mAh/cm^2, 3 mA/cm^2 and 3 mAh/cm^2, and 4 mA/cm^2 and 4 mAh/cm^2 (Fig. 4 and S11), the PVdF-HFP-Li is stable for over 850, 150 and 100 h, respectively, but the bare Li/Li cell starts to fluctuate after less than 50 h. This means that the PVdF-HFP layer can elongate the cycling time by > 100–200% at high current densities. These data clearly demonstrate the effectiveness of the porous PVdF-HFP interlayer.

Besides DOL/DME electrolytes used in Fig. 4, the Li/Li cycling performance is also tested in a EC/DEC electrolyte of 1 M $LiPF_6$ in ethylene carbonate (EC) /diethyl carbonate (DEC) (1:1 v/v) (Fig. 4**c-d** and Figure S12). At 2 mA/cm^2, the PVdF-HFP-Li displays a stable cycling for over 600 cycles, with an overpotential of only 300 mV. However, the overpotential of bare Li start to fluctuate and increase to over 400 mV after only 250 cycles. At 1 mA/cm^2, the PVdF-HFP-Li displays a stable cycling for over 230 cycles, with an overpotential of only 200 mV. However, the overpotential of bare Li start to fluctuate and increase to over 300 mV after only 120 cycles. It also shows the same trend at 3 mA/cm^2. Moreover, the PVdF-HFP-Li only has an overpotential of 270 mV at 2 mA/cm^2 and 2 mAh/cm^2, while the overpotential of bare Li becomes more than 400 mV and fluctuates after only 70 cycles. It can be seen that the electrochemical performance is still better in PVdF-HFP-Li than bare lithium, indicating that this porous structure works well in EC/DEC electrolyte.

The porous PVdF-HFP is further combined with a $LiFePO_4$ cathode to construct a $LiFePO_4$-Li full cell with a cathode capacity of 1.4 mAh/cm^2, as described in the method. A control sample with conventional PE separator is prepared at the same time. Firstly, the $LiFePO_4$/PVdF-HFP-Li full cell shows a much smaller impedance than $LiFePO_4$/bare Li cell (Figure S13c). The charge transfer resistance is reduced from 198 to 73 Ω, which is likely a result of better wetting at the lithium/PVdF-HFP interface. In cycling test at 0.5 C (Fig. 5), the $LiFePO_4$/PVdF-HFP-Li exhibits longer and stable cycling with a capacity of 153 mAh/g for almost 350 cycles without obvious capacity fading. Meanwhile, the $LiFePO_4$/bare Li cell endures a dramatic capacity drop after only 60 cycles and the capacity becomes less than 120 mAh/g at 0.5 C. It could be deduced that the porous structure works well in full cells because of the prevention from forming lithium dendrites and higher CE. The voltage-capacity profile also shows smaller voltage hysteresis of 182 mV in $LiFePO_4$/PVdF-HFP-Li cells compared to 351 mV in $LiFePO_4$/bare Li cells at 0.5 C after 50 cycles. Moreover, the voltage hysteresis even slightly drops from 181 mV at 50th cycle to 159 mV at 200th cycle, and 168 mV at 300th cycle. This suggests that the electrochemical reactions are highly reversible and stable in $LiFePO_4$/PVdF-HFP-Li cell.

4. Conclusions

In summary, a new porous polymer structure is designed and fabricated for the lithium metal anode with highly improved performance. Simulations and experiments show that this structure is effective in suppressing the growth of lithium dendrites. Under the protection of this porous structure, the lithium anode delivers a long cycling life with over 1200 cycles at 3 mA/cm^2 and 1 mAh/cm^2 in Li/Li symmetric cells. The $LiFePO_4$ full cell also displays high cycling stability and high specific capacity. The prohibition in lithium dendrite is effective in Li metal battery, especially in the regime of high current densities. It is expected that this facile design could boost the electrochemical performance, and be further optimized with the aid of ongoing research, such as new electrolytes etc., to enable rechargeable lithium metal batteries with high performance.

Acknowledgements

Y.Y. acknowledges support from startup funding from Columbia University and AFOSR (FA9550-18-1-0410). B. X. acknowledge financial support from China Scholarship Council (CSC) graduate scholarship. We appreciate the help from Lei Chen on phase-field modeling, and Lingyan Shi for Stimulated Raman Scattering Microscopy discussion. This work is supported by Yonghong Zhang Family Center for Advanced Materials for Energy and Environment in Columbia University.

Competing interest

The author declares no competing financial interest.

Appendix A. Supporting information

Supplementary data associated with this article can be found in the online version at doi:10.1016/j.ensm.2018.11.035.

References

[1] M.S. Whittingham, Lithium batteries and cathode materials, Chem. Rev. 104 (2004) 4271–4302.
[2] K. Xu, Electrolytes and interphases in Li-ion batteries and beyond, Chem. Rev. 114 (2014) 11503–11618.
[3] J.C. Bachman, S. Muy, A. Grimaud, H.-H. Chang, N. Pour, S.F. Lux, O. Paschos, F. Maglia, S. Lupart, P. Lamp, L. Giordano, Y. Shao-Horn, Inorganic solid-state electrolytes for lithium batteries: mechanisms and properties governing ion conduction, Chem. Rev. 116 (2016) 140–162.
[4] K. Kang, Y.S. Meng, J. Bréger, C.P. Grey, G. Ceder, Electrodes with high power and high capacity for rechargeable lithium batteries, Science 311 (2006) 977.
[5] J. Lu, Z. Chen, Z. Ma, F. Pan, L.A. Curtiss, K. Amine, The role of nanotechnology in the development of battery materials for electric vehicles, Nat. Nanotechnol. 11 (2016) 1031.

[6] P. Albertus, S. Babinec, S. Litzelman, A. Newman, Status and challenges in enabling the lithium metal electrode for high-energy and low-cost rechargeable batteries, Nat. Energy 3 (2018) 16–21.
[7] Q. Cheng, L. Wei, Z. Liu, N. Ni, Z. Sang, B. Zhu, W. Xu, M. Chen, Y. Miao, L.-Q. Chen, W. Min, Y. Yang, Operando and three-dimensional visualization of anion depletion and lithium growth by stimulated Raman scattering microscopy, Nat. Commun. 9 (2018) 2942.
[8] D. Lin, Y. Liu, Y. Cui, Reviving the lithium metal anode for high-energy batteries, Nat. Nanotechnol. 12 (2017) 194.
[9] Y. Lu, Z. Tu, L.A. Archer, Stable lithium electrodeposition in liquid and nanoporous solid electrolytes, Nat. Mater. 13 (2014) 961.
[10] W. Xu, J. Wang, F. Ding, X. Chen, E. Nasybulin, Y. Zhang, J.-G. Zhang, Lithium metal anodes for rechargeable batteries, Energy Environ. Sci. 7 (2014) 513–537.
[11] J. Lang, L. Qi, Y. Luo, H. Wu, High performance lithium metal anode: progress and prospects, Energy Storage Mater. 7 (2017) 115–129.
[12] X. Shen, H. Liu, X.-B. Cheng, C. Yan, J.-Q. Huang, Beyond lithium ion batteries: higher energy density battery systems based on lithium metal anodes, Energy Storage Mater. 12 (2018) 161–175.
[13] G. Zheng, S.W. Lee, Z. Liang, H.-W. Lee, K. Yan, H. Yao, H. Wang, W. Li, S. Chu, Y. Cui, Interconnected hollow carbon nanospheres for stable lithium metal anodes, Nat. Nanotechnol. 9 (2014) 618.
[14] B. Zhu, Y. Jin, X. Hu, Q. Zheng, S. Zhang, Q. Wang, J. Zhu, Poly(dimethylsiloxane) thin film as a stable interfacial layer for high-performance lithium-metal battery anodes, Adv. Mater. 29 (2016) 1603755.
[15] S. Liu, X. Xia, Y. Zhong, S. Deng, Z. Yao, L. Zhang, X.-B. Cheng, X. Wang, Q. Zhang, J. Tu, 3D TiC/C core/shell nanowire skeleton for dendrite-free and long-life lithium metal anode, Adv. Energy Mater. 8 (2017) 1702322.
[16] H. Ye, S. Xin, Y.X. Yin, J.Y. Li, Y.G. Guo, L.J. Wan, Stable Li plating/stripping electrochemistry realized by a hybrid li reservoir in spherical carbon granules with 3D conducting skeletons, J Am. Chem. Soc. 139 (2017) 5916–5922.
[17] Y. Zhang, W. Luo, C. Wang, Y. Li, C. Chen, J. Song, J. Dai, E.M. Hitz, S. Xu, C. Yang, Y. Wang, L. Hu, High-capacity, low-tortuosity, and channel-guided lithium metal anode, Proc. Natl. Acad. Sci. USA 11 (4) (2017) 3584.
[18] X. Li, J. Zheng, X. Ren, M.H. Engelhard, W. Zhao, Q. Li, J.-G. Zhang, W. Xu, Dendrite-free and performance-enhanced lithium metal batteries through optimizing solvent compositions and adding combinational additives, Adv. Energy Mater. 8 (2018) 1703022.
[19] C.-P. Yang, Y.-X. Yin, S.-F. Zhang, N.-W. Li, Y.-G. Guo, Accommodating lithium into 3D current collectors with a submicron skeleton towards long-life lithium metal anodes, Nat. Commun. 6 (2015) 8058.
[20] Q. Yun, Y.-B. He, W. Lv, Y. Zhao, B. Li, F. Kang, Q.-H. Yang, Chemical dealloying derived 3D porous current collector for Li metal anodes, Adv. Mater. 28 (2016) 6932–6939.
[21] H. Ye, Y.-X. Yin, S.-F. Zhang, Y. Shi, L. Liu, X.-X. Zeng, R. Wen, Y.-G. Guo, L.-J. Wan, Synergism of Al-containing solid electrolyte interphase layer and Al-based colloidal particles for stable lithium anode, Nano Energy 36 (2017) 411–417.
[22] X. Liang, Q. Pang, I.R. Kochetkov, M.S. Sempere, H. Huang, X. Sun, L.F. Nazar, A facile surface chemistry route to a stabilized lithium metal anode, Nat. Energy 2 (2017) 17119.
[23] K. Liao, S. Wu, X. Mu, Q. Lu, M. Han, P. He, Z. Shao, H. Zhou, Developing a "water-defendable" and "dendrite-free" lithium-metal anode using a simple and promising GeCl4 pretreatment method, Adv. Mater. 30 (2018) 1705711.
[24] K. Yan, H.-W. Lee, T. Gao, G. Zheng, H. Yao, H. Wang, Z. Lu, Y. Zhou, Z. Liang, Z. Liu, S. Chu, Y. Cui, Ultrathin Two-dimensional atomic crystals as stable interfacial layer for improvement of lithium metal anode, Nano Lett. 14 (2014) 6016–6022.
[25] M.-H. Ryou, D.J. Lee, J.-N. Lee, Y.M. Lee, J.-K. Park, J.W. Choi, Excellent cycle life of lithium-metal anodes in lithium-ion batteries with mussel-inspired polydopamine-coated separators, Adv. Energy Mater. 2 (2012) 645–650.
[26] L. Suo, Y.-S. Hu, H. Li, M. Armand, L. Chen, A new class of solvent-in-salt electrolyte for high-energy rechargeable metallic lithium batteries, Nat. Commun. 4 (2013) 1481.
[27] L. Suo, W. Xue, M. Gobet, S.G. Greenbaum, C. Wang, Y. Chen, W. Yang, Y. Li, J. Li, Fluorine-donating electrolytes enable highly reversible 5-V-class Li metal batteries, Proc. Natl. Acad. Sci. USA (2018).
[28] J. Zheng, M.H. Engelhard, D. Mei, S. Jiao, B.J. Polzin, J.-G. Zhang, W. Xu, Electrolyte additive enabled fast charging and stable cycling lithium metal batteries, Nat. Energy 2 (2017) 17012.
[29] C.-Z. Zhao, X.-B. Cheng, R. Zhang, H.-J. Peng, J.-Q. Huang, R. Ran, Z.-H. Huang, F. Wei, Q. Zhang, Li2S5-based ternary-salt electrolyte for robust lithium metal anode, Energy Storage Mater. 3 (2016) 77–84.
[30] K. Fu, Y. Gong, J. Dai, A. Gong, X. Han, Y. Yao, C. Wang, Y. Wang, Y. Chen, C. Yan, Y. Li, E.D. Wachsman, L. Hu, Flexible, solid-state, ion-conducting membrane with 3D garnet nanofiber networks for lithium batteries, Proc. Natl. Acad. Sci. USA 11 (3) (2016) 7094.
[31] F. Han, J. Yue, C. Chen, N. Zhao, X. Fan, Z. Ma, T. Gao, F. Wang, X. Guo, C. Wang, Interphase engineering enabled all-ceramic lithium battery, Joule 2 (2018) 497–508.
[32] X. Zhang, T. Liu, S. Zhang, X. Huang, B. Xu, Y. Lin, B. Xu, L. Li, C.-W. Nan, Y. Shen, Synergistic coupling between Li6.75La3Zr1.75Ta0.25O12 and poly(vinylidene fluoride) induces high ionic conductivity, mechanical strength, and thermal stability of solid composite electrolytes, J. Am. Chem. Soc. 139 (2017) 13779–13785.
[33] P. Yao, B. Zhu, H. Zhai, X. Liao, Y. Zhu, W. Xu, Q. Cheng, C. Jayyosi, Z. Li, J. Zhu, K.M. Myers, X. Chen, Y. Yang, PVDF/palygorskite nanowire composite electrolyte for 4 V rechargeable lithium batteries with high energy density, Nano Lett. 18 (2018) 6113–6120.
[34] H. Zhai, P. Xu, M. Ning, Q. Cheng, J. Mandal, Y. Yang, A flexible solid composite electrolyte with vertically aligned and connected ion-conducting nanoparticles for lithium batteries, Nano Lett. 17 (2017) 3182–3187.
[35] X.-B. Cheng, R. Zhang, C.-Z. Zhao, F. Wei, J.-G. Zhang, Q. Zhang, A review of solid electrolyte interphases on lithium metal anode, Adv. Sci. 3 (2015) 1500213.
[36] C.W. Freudiger, W. Min, B.G. Saar, S. Lu, G.R. Holtom, C. He, J.C. Tsai, J.X. Kang, X.S. Xie, Label-free biomedical imaging with high sensitivity by stimulated raman scattering microscopy, Science 322 (2008) 1857.
[37] L. Chen, H.W. Zhang, L.Y. Liang, Z. Liu, Y. Qi, P. Lu, J. Chen, L.-Q. Chen, Modulation of dendritic patterns during electrodeposition: a nonlinear phase-field model, J. Power Sources 300 (2015) 376–385.